scientific reports

Check for updates

OPEN

Higher-order topological insulator in cubic semiconductor quantum wells

Sergey S. Krishtopenko

The search for exotic new topological states of matter in widely accessible materials, for which the manufacturing process is mastered, is one of the major challenges of the current topological physics. Here we predict higher order topological insulator state in quantum wells based on the most common semiconducting materials. By successively deriving the bulk and boundary Hamiltonians, we theoretically prove the existence of topological corner states due to cubic symmetry in quantum wells with double band inversion. We show that the appearance of corner states does not depend solely on the crystallographic orientation of the meeting edges, but also on the growth orientation of the quantum well. Our theoretical results significantly extend the application potential of topological quantum wells based on IV, II–VI and III–V semiconductors with diamond or zinc-blende structures.

Since the discovery of $\mathbb{Z}_2$ topological insulators (TIs)[1,2], topological phases and materials have been extensively explored in two- (2D) and three-dimensional (3D) systems[3–5]. The recent classification[6–8] of TIs with given crystalline symmetry has led to the discovery of a new type of topological phases, the higher-order topological insulators (HOTIs)[9–15]. The 3D HOTIs are gapped in the bulk and on all surfaces, but they have one-dimensional (1D) gapless modes along "hinges", where two surfaces meet. These hinge states were experimentally observed in bismuth[16], Bi_4Br_4[17] and WTe_2 crystals[18,19] and theoretically predicted for strained SnTe[12], transition metal dichalcogenides XTe_2[20] and antiperovskites[21].

In 2D HOTIs, pioneering works[9,10,13] suggest the presence of zero-dimensional (0D) corner states inside the insulating edge and bulk band-gap of certain materials. Recently, Peterson et al.[22] have shown that 0D corner states may reside either in the bulk band-gap or fully within the bulk bands of a HOTI, depending on the material's details. HOTIs that fall into the latter case do not host 0D corner states within their bulk band-gap and, as such, cannot be distinguished from trivial insulators by their spectrum alone. Nevertheless, even in this case the higher-order topology can be still identified via a fractional corner anomaly[22,23].

So far, a large part of the experimental study of 2D HOTIs has been performed in engineered metamaterials[24–34], while only a few candidates have been theoretically predicted in solids, including black phosphorene[35], graphdiyne[36], bismuthene[37] and twisted bilayer graphene at certain angles[38]. Although twisted bilayer graphene can be indeed a realistic candidate to probe 2D HOTI state experimentally, it is still highly desirable to identify controllable and widely accessible higher-order topological materials.

Nowadays, many technologically important semiconductors with the most developed molecular-beam-epitaxy growth hold a cubic crystal structure, including the diamond structure for the group-IV elements, and the zinc-blend structure for the III–V and II–VI compounds. For instance, the time-reversal-invariant 2D TI state, also known as quantum spin Hall insulator (QSHI)—was first discovered in the cubic semiconductor QWs with an inverted band structure: HgTe/CdHgTe QWs[2,39] and broken-gap InAs/GaSb QW bilayers[40,41]. Later, InN/GaN QWs[42], Ge/GaAs QWs[43] and InAsBi/AlSb QWs[44] were also predicted to be 2D TIs. Such a list can be obviously extended by including variety of type-II broken-gap QW heterostructures[45–48] (similar to the InAs/GaSb QWs) on the basis of III–V semiconductors and their alloys.

This work shows that in addition to "conventional" first-order 2D TI state, cubic IV, III–V and II–VI semiconductors are also promising for the implementation of time-reversal-invariant 2D HOTI. Starting from realistic multi-band $\mathbf{k}\cdot\mathbf{p}$ Hamiltonian[49], we directly derive an effective 2D low-energy Hamiltonian preserving the cubic symmetry of the semiconductors. Then, by applying open boundary conditions, we obtain an effective 1D Hamiltonian for the edge states and demonstrate the existence of the corner states in the QWs with double band

[1]CENTERA Laboratories, Institute of High Pressure Physics, Polish Academy of Sciences, 01-142 Warsaw, Poland. [2]Laboratoire Charles Coulomb (L2C), UMR 5221 CNRS-Université de Montpellier, 34095 Montpellier, France. email: sergey.krishtopenko@gmail.com

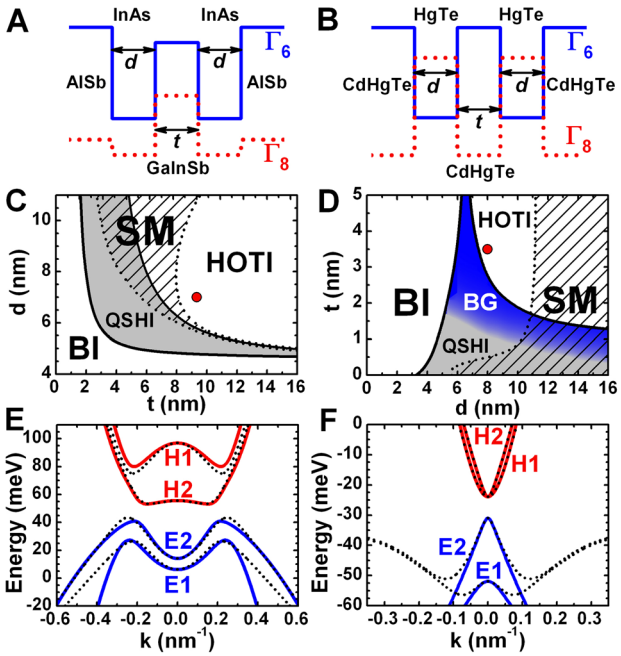

Figure 1. Band structure of three-layer InAs/GaInSb and double HgTe/CdHgTe QWs. (**A**) Schematic representation of symmetrical three-layer InAs/$Ga_{0.65}In_{0.35}Sb$ QW confined by outer AlSb barriers[50]. Here, *d* and *t* are the thicknesses of InAs and $Ga_{0.65}In_{0.35}Sb$ layers, respectively. The QW is supposed to be grown on (001) GaSb buffer. (**B**) Schematic representation of double HgTe/$Cd_{0.7}Hg_{0.3}Te$ QW. Here, *d* is the thickness of HgTe layers and *t* is the middle CdHgTe barrier thickness. The double QW is assumed to be grown on (001) CdTe buffer. The Hg content in all the barriers is chosen to be 0.3[51]. (**C**,**D**) The phase diagrams for different *d* and *t*. The left-hand and right-hand solid curves correspond to the crossing between *E*1–*H*1 subbands and *E*2–*H*2 subbands, respectively. These curves divide the plane into three parts with trivial band ordering corresponding to band insulator (BI, see the left-hand white region), single band inversion (grey and blue regions) and double-band inversion (right-hand white region). The striped region defines a semimetal (SM) phase with vanishing *indirect* band-gap[50,51]. (**E**,**F**) Band structure calculated on the basis of effective 2D low-energy Hamiltonian for the QWs with the layer thicknesses marked by the red symbols in (**B**) and (**C**). The blue and red curves represent band dispersion of electron-like and hole-like subbands, respectively. The wave vector is oriented along (100) crystallographic direction. The dotted curves represent the calculations based on realistic multi-band $\mathbf{k}\cdot\mathbf{p}$ Hamiltonian[49] .

inversion. As two prototype 2D systems, we consider three-layer InAs/GaInSb QWs[50] and double HgTe/CdHgTe QWs[51] grown along (0*mn*) crystallographic orientations (where *m* and *n* are integers).

Results

Insulating state with double band inversion. Let us first explore the possibility for double band inversion in the prototype QWs (see Fig. 1). Since these QWs can be considered as two tunnel-coupled HgTe QWs[2,39] or InAs/GaInSb QW bilayers[40,41], each of which features a single band inversion, the appearance of double band inversion is not surprising for such multi-layer systems. In Fig. 1C,D, we provide a phase diagram for three-layer InAs/$Ga_{0.65}In_{0.35}Sb$ and double HgTe/$Cd_{0.7}Hg_{0.3}Te$ QWs with different layer thicknesses. Both QWs are supposed to be grown on the (001) crystallographic plane.

In the diagrams, the left-hand black solid curve describing the crossing between the first electron-like (*E*1) and hole-like (*H*1) subbands divides the *d*-*t* plane into a white region, corresponding to band insulator (BI) with trivial band ordering, and a grey region of QSHI with inverted band structure. If the middle barrier is thick enough, in addition to QSHI, the double HgTe/CdHgTe QWs also hold a specific state with a band structure similar to the one of bilayer graphene (BG) (see the blue region in Fig. 1D). A detailed discussion of the "bilayer graphene" state can be found in[51].

Further increasing of *d* and *t* results in the band crossing between the second electron-like (*E*2) and hole-like (*H*2) subbands, which is shown by the right-hand black solid curve in the diagram. This curve, in its turn, separates the grey and blue regions with single band inversion from the right-hand white region corresponding to the double band inversion, when two electron-like *E*1 and *E*2 levels lie below two hole-like *H*1 and *H*2 subbands.

Finally, at certain *d* and *t* values, corresponding to the striped region, the so-called semimetal (SM) phase is implemented. The semimetal phase is characterized by a vanishing *indirect* band-gap when the side maxima of the valence subband exceed in energy the conduction subband bottom[50,51]. Thus, by varying the layer thicknesses in the prototype QWs, one can indeed realize band insulator, QSHI (or "bilayer graphene" state), semimetal

phase and the insulator state with a double band inversion. In this work, we identify a double-band-inversion insulator state 2D HOTI with the corner states arising due to cubic symmetry of II–VI and III–V semiconductors.

To describe double band inversion at the Γ point of the Brillouin zone, we derive an effective 2D low-energy Hamiltonian taking into account $E1$, $E2$, $H1$ and $H2$ subbands and preserving the cubic symmetry of the prototype QWs. Starting from a realistic multi-band $\mathbf{k}\cdot\mathbf{p}$ Hamiltonian for $(0mn)$-oriented cubic semiconductor QWs[49] and following expansion procedure described in the Supplementary Materials, in the basis $|E1+\rangle, |H1+\rangle, |H2-\rangle, |E2-\rangle, |E1-\rangle, |H1-\rangle, |H2+\rangle, |E2+\rangle$, the effective 2D Hamiltonian in the vicinity of the Γ point has the form:

$$H_{2D}(k_x,k_y)=\begin{pmatrix} H_{4\times4}(k_x,k_y) & 0 \\ 0 & H^{*}_{4\times4}(-k_x,-k_y)\end{pmatrix}, \tag{1}$$

where the asterisk denotes complex conjugation. The diagonal blocks of $H_{2D}(k_x,k_y)$ are split into isotropic and anisotropic parts:

$$H_{4\times4}(k_x,k_y)=H^{(i)}_{4\times4}(k_x,k_y)+H^{(a)}_{4\times4}(k_x,k_y). \tag{2}$$

The isotropic part $H^{(i)}_{4\times4}(k_x,k_y)$ is written as[52,53]:

$$H^{(i)}_{4\times4}(k_x,k_y)=\begin{pmatrix} \epsilon_{E1} & -A_1k_+ & R^{(i)}_1k_-^2 & S_0k_- \\ -A_1k_- & \epsilon_{H1} & 0 & R^{(i)}_2k_-^2 \\ R^{(i)}_1k_+^2 & 0 & \epsilon_{H2} & A_2k_+ \\ S_0k_+ & R^{(i)}_2k_+^2 & A_2k_- & \epsilon_{E2}\end{pmatrix}, \tag{3}$$

where

$$\begin{aligned}\epsilon_{E1}(k_x,k_y)&=C_1+M_1-(D_1+B_1)(k_x^2+k_y^2),\\ \epsilon_{H1}(k_x,k_y)&=C_1-M_1-(D_1-B_1)(k_x^2+k_y^2),\\ \epsilon_{E2}(k_x,k_y)&=C_2+M_2-(D_2+B_2)(k_x^2+k_y^2),\\ \epsilon_{H2}(k_x,k_y)&=C_2-M_2-(D_2-B_2)(k_x^2+k_y^2).\end{aligned} \tag{4}$$

Here, $k_\pm=k_x\pm ik_y$, k_x and k_y are the momentum components in the QW plane, and $C_{1,2}$, $M_{1,2}$, $A_{1,2}$, $B_{1,2}$, $D_{1,2}$, S_0 and $R^{(i)}_{1,2}$ are *isotropic* structure parameters being defined by the QW geometry, the growth orientation and the materials. The Hamiltonian $H_{2D}(k_x,k_y)$ has a block-diagonal form because we keep the inversion symmetry (see Supplementary Materials) by neglecting the terms resulting from the anisotropy of chemical bonds at the QW interfaces[54] and the bulk inversion asymmetry of the unit cell of zinc-blende semiconductors[55]. The latter is absent for diamond-like semiconductors.

The most important quantities in $H_{2D}(k_x,k_y)$ are two mass parameters M_1 and M_2 describing the band inversion between $E1$–$H1$ subbands and $E2$–$H2$ subbands, respectively. The trivial band insulator corresponds to positive values of M_1 and M_2. The QSHI and "bilayer graphene" states arise if $M_1<0$ and $M_2>0$, and the difference between these states is defined by the gap between $H1$ and $H2$ subbands, which is zero in the case of "bilayer graphene" state[51]. The insulator state with double band inversion is defined by the negative values of M_1 and M_2. We note that since the semimetal phase represented by the striped areas in the diagrams is formed by non-local overlapping of the valence and conduction subbands, it cannot be described within the low-energy Hamiltonian for the small values of k_x and k_y.

The isotropic term $H^{(i)}_{4\times4}(k_x,k_y)$ preserves the rotational symmetry in the QW plane, therefore it is independent of the orientation of x and y axis. In contrast, the form of the anisotropic term $H^{(a)}_{4\times4}(k_x,k_y)$ in Eq. (2), resulting from the cubic symmetry of diamond and zinc-blende semiconductors, depend not only on the QW growth orientation but also on the orientation of x and y axis (see Supplementary Materials). For $(0mn)$-oriented QWs, $H^{(a)}_{4\times4}(k_x,k_y)$ has the form

$$\begin{aligned}H^{(a)}_{4\times4}(k_x,k_y)=&-\begin{pmatrix} 0 & 0 & R^{(a)}_1e^{i4\varphi}k_+^2 & 0 \\ 0 & 0 & 0 & R^{(a)}_2e^{i4\varphi}k_+^2 \\ R^{(a)}_1e^{-i4\varphi}k_-^2 & 0 & 0 & 0 \\ 0 & R^{(a)}_2e^{-i4\varphi}k_-^2 & 0 & 0\end{pmatrix}\\ &-\left(k_y\cos\varphi+k_x\sin\varphi\right)^2\sin^2 2\theta\begin{pmatrix} 0 & 0 & R^{(a)}_1e^{i2\varphi} & 0 \\ 0 & 0 & 0 & R^{(a)}_2e^{i2\varphi} \\ R^{(a)}_1e^{-i2\varphi} & 0 & 0 & 0 \\ 0 & R^{(a)}_2e^{-i2\varphi} & 0 & 0\end{pmatrix}\\ &+\sin 2\theta\begin{pmatrix} 0 & 0 & \tilde{R}^{(a)}_1e^{i2\varphi} & 0 \\ 0 & 0 & 0 & \tilde{R}^{(a)}_2e^{i2\varphi} \\ \tilde{R}^{(a)}_1e^{-i2\varphi} & 0 & 0 & 0 \\ 0 & \tilde{R}^{(a)}_2e^{-i2\varphi} & 0 & 0\end{pmatrix},\end{aligned} \tag{5}$$

where $R^{(a)}_{1,2}$ and $\tilde{R}^{(a)}_{1,2}$ are *cubic* structure parameters, which depend on the QW geometry and materials. In Eq. (5), $\theta = \arctan(m/n)$ is the angle defining the QW growth orientation, while the angle φ is the angle between the x axis and the (001) crystallographic direction.

As clear from above, depending on the structure parameters, the effective 2D Hamiltonian in Eq. (1) describes QSHI, "bilayer-graphene" state, trivial band insulator or insulator with double band inversion. Note that thirteen parameters involved in $H_{2D}(k_x, k_y)$ cannot take arbitrary values. Since their calculation is based on the wave-functions of the multi-band $\mathbf{k}\cdot\mathbf{p}$ Hamiltonian at $k_x = k_y = 0$ (for details, see Supplementary Materials), the set of parameters corresponding to specific topological state is determined by the thicknesses and materials of the QW layers, its growth orientation, and the buffer on which the QW is grown. The latter is crucial for taking into account the effect of lattice-mismatch strain on the band structure in the QW. Thus, all of the structure parameters are the functions of d, t, m, n and the QW layer and buffer materials. Further, we perform the calculations for two sets of structure parameters involved in $H_{2D}(k_x, k_y)$, which correspond to the prototype QWs with the layer thicknesses marked by the red symbols in Fig. 1C,D. Figure 1E,F compare the band structure calculations based on realistic multi-band $\mathbf{k}\cdot\mathbf{p}$ Hamiltonian[49] and $H_{2D}(k_x, k_y)$ in Eq. (1). The isotropic and cubic structure parameters of $H_{2D}(k_x, k_y)$ for the insulator state with double band inversion are given in the Supplementary Materials.

Anisotropic edge states. Let us now analyze the edge states arising in the insulator with double band inversion. Since $H_{2D}(k_x, k_y)$ in Eq. (1) has block-diagonal form, we further focus on the upper block $H_{4\times4}(k_x, k_y)$ only, while the calculations for the lower block $H^*_{4\times4}(-k_x, -k_y)$ can be performed in the similar manner.

To derive an effective 1D low-energy edge Hamiltonian, we split $H_{2D}(k_x, k_y)$ into two parts so that the first part represents two independent BHZ-like models[2] with $M_1 < 0$ and $M_2 < 0$ for the pairs of $E1$–$H1$ subbands and $E2$–$H2$ subbands, while the second part includes the rest isotropic and cubic terms describing the inter-pairs mixing. Then, assuming open-boundary conditions in a semi-infinite plane $y > 0$, we solve the eigenvalue problem for the independent BHZ-like blocks to find the edge wave-functions at $k_x = 0$. In this case, the edge orientation represented by the x axis is defined by the angle φ measured from (100) crystallographic direction. Finally, we construct a low-energy edge Hamiltonian by projecting $H_{4\times4}(k_x, k_y)$ onto the obtained set of the basis edge functions (see Supplementary Materials).

The projection of two independent BHZ-like blocks[2] with non-zero k_x leads to

$$H^{(0)}_{1D}(k_x) = \begin{pmatrix} C_1 - \dfrac{M_1 D_1}{B_1} - \dfrac{2A_1\eta_1}{1+\eta_1^2}k_x & 0 \\ 0 & C_2 - \dfrac{M_2 D_2}{B_2} + \dfrac{2A_2\eta_2}{1+\eta_2^2}k_x \end{pmatrix}, \tag{6}$$

where $\eta_n^2 = (B_n + D_n)/(B_n - D_n)$ with $n = 1$ and 2 corresponding to the pairs of $E1$-$H1$ and $E2$-$H2$ subbands, respectively. One can see that $H^{(0)}_{1D}(k_x)$ describes the linear edge dispersion due to the inversion of the subband pairs $|E1,+\rangle$-$|H1,+\rangle$ and $|E2,-\rangle$-$|H2,-\rangle$ in the absence of their mixing[56]. The two energy branches cross at $k_x = k_c$:

$$k_c = \frac{C_1 - C_2 + \dfrac{M_2 D_2}{B_2} - \dfrac{M_1 D_1}{B_1}}{\dfrac{2A_1\eta_1}{1+\eta_1^2} + \dfrac{2A_2\eta_2}{1+\eta_2^2}}, \tag{7}$$

that allows the representation of $H^{(0)}_{1D}(k_x)$ in the form of the Hamiltonian of 'tilted" 1D massless Dirac fermions:

$$H^{(0)}_{1D}(k_x) = \varepsilon_0 + v_0\delta k\mathbf{I}_2 + v_z\delta k\sigma_z, \tag{8}$$

where $\delta k = k_x - k_c$, $\mathbf{I}_2$ is a 2×2 identity matrix, σ_z is one of the Pauli matrices, and ε_0 is a constant corresponding to the energy of the crossing point at $k_x = k_c$. In Eq. (8), v_0 and v_z are written as

$$v_0 = \frac{A_1\eta_1}{1+\eta_1^2} - \frac{A_2\eta_2}{1+\eta_2^2},$$
$$v_z = \frac{A_1\eta_1}{1+\eta_1^2} + \frac{A_2\eta_2}{1+\eta_2^2}.$$

Note that the crossing of other Kramer's partners occurs at $k_x = -k_c$.

The projection of the rest terms of $H_{4\times4}(k_x, k_y)$ representing the mixing between the pairs $|E1,+\rangle$-$|H1,+\rangle$ and $|E2,-\rangle$-$|H2,-\rangle$ results in anti-diagonal mass terms describing the band-gap opening. After straightforward calculations with the details provided in the Supplementary Materials, we finally obtain the low-energy 1D edge Hamiltonian:

$$H_{1D}(\delta k, \theta, \varphi) = \varepsilon_0 + v_0\delta k\mathbf{I}_2 + v_z\delta k\sigma_z + \left(m_y + v_y\delta k + \delta_y\delta k^2\right)\sigma_y + \left(m_x + v_x\delta k + \delta_x\delta k^2\right)\sigma_x, \tag{9}$$

where $v_x, v_y, m_x, m_y, \delta_x, \delta_y$ include the angle dependence on θ and φ:

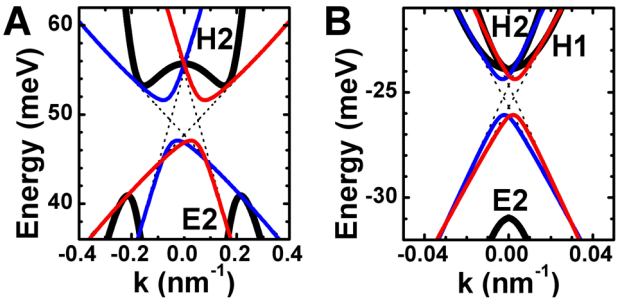

Figure 2. Energy dispersion of the bulk and edge states in the prototype QWs with double band inversion. The (**A**) and (**B**) presents the calculations based on low-energy 1D and 2D Hamiltonians for the (001)-oriented three-layer InAs/GaInSb and double HgTe/CdHgTe QWs, respectively. The layer thicknesses of the prototype QWs are marked by the red symbols in Fig. 1B,C. Bulk states being described by $H_{2D}(k_x, k_y)$ in Eq. (1) are shown in black. Red and blue curves correspond to different Kramer's partners of the edge states. The dashed curves are the eigenvalues of $H_{1D}^{(0)}(k_x)$ in Eq. (8). The wave vector and the edge are oriented along (100) crystallographic direction.

$$
\begin{aligned}
m_x &= F_a\kappa_2\cos 4\varphi - F_i\kappa_2 - F_0\kappa_1 + (F_i - F_a\cos 4\varphi)k_c^2\\
&\quad + [F_0 - 2\kappa_1(F_i + F_a\cos 4\varphi)]k_c + \tilde{F}_a\cos 2\varphi\sin 2\theta\\
&\quad - F_a\cos 2\varphi\sin^2 2\theta\left(k_c^2\sin^2\varphi + \kappa_2\cos^2\varphi\right)\\
&\quad - F_a\kappa_1 k_c\sin^2 2\varphi\sin^2 2\theta,\\
m_y &= F_a\sin 4\varphi\left[k_c^2 + 2\kappa_1 k_c - \kappa_2\right] - \tilde{F}_a\sin 2\varphi\sin 2\theta\\
&\quad + F_a\sin 2\varphi\sin^2 2\theta\left(k_c^2\sin^2\varphi - \kappa_1 k_c\cos 2\varphi + \kappa_2\cos^2\varphi\right),\\
v_x &= F_0 + 2k_c(F_i - F_a\cos 4\varphi) - 2\kappa_1(F_i + F_a\cos 4\varphi)\\
&\quad - F_a\sin^2 2\theta\left(2k_c\cos 2\varphi\sin^2\varphi + \kappa_1\sin^2 2\varphi\right),\\
v_y &= 2F_a\sin 4\varphi(\kappa_1 + k_c)\\
&\quad + F_a\sin 2\varphi\sin^2 2\theta\left(2k_c\sin^2\varphi - \kappa_1\cos 2\varphi\right),\\
\delta_x &= F_i - F_a\cos 4\varphi - F_a\cos 2\varphi\sin^2\varphi\sin^2 2\theta,\\
\delta_y &= F_a\sin 4\varphi + F_a\sin 2\varphi\sin^2\varphi\sin^2 2\theta.
\end{aligned}
\tag{10}
$$

Here, κ_1 and κ_2 are defined by the matrix elements $\langle\partial/\partial y\rangle$ and $\langle\partial^2/\partial y^2\rangle$, respectively, both calculated by using the basis edge functions at $k_x = 0$ (see Supplementary Materials). In Eqs. (10), we have also introduced the edge *isotropic* (F_i, F_0) and *cubic* (F_a, $\tilde{F}_a$) parameters:

$$
\begin{aligned}
F_i &= \frac{R_1^{(i)}\eta_2 + R_2^{(i)}\eta_1}{\sqrt{1+\eta_1^2}\sqrt{1+\eta_2^2}}, \qquad F_0 = \frac{S_0}{\sqrt{1+\eta_1^2}\sqrt{1+\eta_2^2}},\\
F_a &= \frac{R_1^{(a)}\eta_2 + R_2^{(a)}\eta_1}{\sqrt{1+\eta_1^2}\sqrt{1+\eta_2^2}}, \qquad \tilde{F}_a = \frac{\tilde{R}_1^{(a)}\eta_2 + \tilde{R}_2^{(a)}\eta_1}{\sqrt{1+\eta_1^2}\sqrt{1+\eta_2^2}}.
\end{aligned}
\tag{11}
$$

The similar calculations for the block $H_{4\times4}^*(-k_x, -k_y)$ in Eq. (1) results in $H_{1D}^*(-k_x - k_c, \theta, \varphi)$. The parameters $v_x, v_y, m_x, m_y, \delta_x, \delta_y$ as a function of the edge orientation φ for the prototype QWs grown along (001), (011) and (013) crystallographic directions are provided in the Supplementary Materials.

Figure 2 shows the edge state picture of the prototype QWs with double band inversion based on low-energy 1D edge Hamiltonian for the edge oriented along (100) crystallographic direction, i.e. $\varphi = 0$. One can see that the edge dispersion of each Kramer's partner mimics the dispersion of "tilted" 1D massive Dirac fermions. However, an important distinctive property of the edge states shown in Fig. 2 is that their gap is described simultaneously by two mass m_x and m_y parameters that prevent the gap vanishing at specific edge orientation (cf. Refs.[35–38]). Indeed, if one neglects the cubic terms of $H_{2D}(k_x, k_y)$, resulting in $F_a = \tilde{F}_a = 0$ in Eq. (10), the mass parameter m_y vanishes, while m_x becomes independent of the edge orientation. Nevertheless, even such complex structure of the edge states yields the corner states in prototype QWs with double band inversion.

0D corner states and boundary conditions. To calculate the energy of the corner states, we apply linear approximation of the effective low-energy 1D edge Hamiltonian $H_{1D}(\delta k, \theta, \varphi)$. Before going further, we should make a certain remark simplifying the calculations. With the parameters provided in the Supplementary Materials, one can verify that both v_x and v_y are significantly lower than v_0 and v_z for any orientation of the edges (also

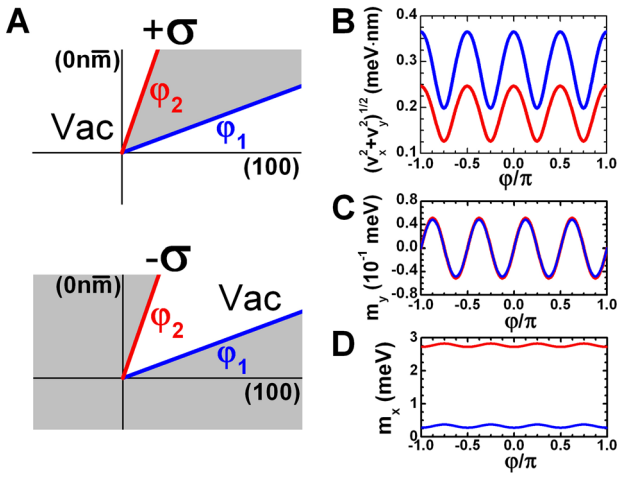

Figure 3. Orientation of the corner edge of (0mn)-oriented prototype QWs. (**A**) Schematic of two edges with a common corner with respect to main crystallographic axes in the QW plane. The sample and external vacuum are shown in grey and white, respectively. External and internal angles differ by the parameter $+\sigma$ and $-\sigma$ (see the text). (**B**–**D**) Dependence of m_x, m_y and $\sqrt{v_x^2+v_y^2}$ on the edge orientation φ for the (001)-oriented three-layer InAs/GaInSb (in red) and double HgTe/CdHgTe QW (in blue) with the layer thicknesses marked by the red symbols in Fig. 1B,C. The edge independent parameters (v_0, v_z) equal to (36.6, 68.1) meV nm and (−16.9, 200.3) meV nm for the three-layer InAs/GaInSb and double HgTe/CdHgTe QW, respectively. This means a good approximation of $\sqrt{v_x^2+v_y^2} \ll |v_0|, |v_z|$ for both QWs.

see Fig. 3). Therefore, one can neglect these terms in the first approximation and take them into account by means of perturbation theory.

Thus, by applying the unitary transformation, the linear part of Eq. (9) can be written as

$$\tilde{H}_{1D}(\delta k) = \varepsilon_0 + v_0 \delta k \mathbf{I}_2 - v_z \delta k \sigma_y - m_y \sigma_z - m_x \sigma_x. \tag{12}$$

It is clear that Eq. (12) represents a 1D Dirac Hamiltonian with the mass $-m_y$, which changes its sign with φ (see Fig. 3), modified by the presence of "tilted" term $v_0 \delta k \mathbf{I}_2$ and second mass term $m_x \sigma_x$.

Let us now define the coordinate x along the curved edge so that $x = 0$ corresponds to the meeting corner as shown in Fig. 3A. The latter means that m_x, m_y in Eq. (12) are the function of x, and $\delta k = -i\partial/\partial x$. Note that $\tilde{H}_{1D}(-i\partial/\partial x)$ is defined in disjoint regions out of $x = 0$. To fully define the 1D system, one needs to specify the boundary conditions that the wave functions must satisfy in the vicinity of $x = 0$.

As shown in the Supplementary Materials, the general *linear* boundary condition, conserving the probability current along the curved edge, can be written in the form

$$e^{-i\beta_1\sigma_y}\Phi_1\big|_{x=-0} = e^{-i\beta_2\sigma_y}\Phi_2\big|_{x=+0}, \tag{13}$$

where Φ_1 and Φ_2 are the wave-functions defined from different sides of the corner, while β_1 and β_2 are real parameters lying in the range from $-\pi/2$ to $\pi/2$. A physical interpretation of these parameters will be discussed later.

On the basis of Eq. (13), it is convenient to introduce a new Hamiltonian $H_{1D}^{(new)} = e^{i\tilde{\beta}\sigma_y}\tilde{H}_{1D}e^{-i\tilde{\beta}\sigma_y}$, whose eigenfunctions $\Psi_{0D}(x)$ are continuous at $x = 0$:

$$H_{1D}^{(new)}(\delta k, x, \tilde{\beta}) = \varepsilon_0 + v_0 \hat{k} \mathbf{I}_2 - v_z \hat{k} \sigma_y + M_z(x, \tilde{\beta})\sigma_z - M_x(x, \tilde{\beta})\sigma_x, \tag{14}$$

where $M_z(x)$ and $M_x(x)$ are

$$\begin{aligned} M_z(x, \tilde{\beta}) &= m_x(x) \sin 2\tilde{\beta} - m_y(x) \cos 2\tilde{\beta}, \\ M_x(x, \tilde{\beta}) &= m_x(x) \cos 2\tilde{\beta} + m_y(x) \sin 2\tilde{\beta} \end{aligned} \tag{15}$$

with $\tilde{\beta}$ also being a function of x.

In view of the above, the Schrödinger equation for the corner states takes the form

$$\left(-v_z \delta k \sigma_y + M_z \sigma_z - M_x \sigma_x\right)\Psi_{0D}(x) = (E - \varepsilon_0 - v_0 \delta k)\mathbf{I}_2 \Psi_{0D}(x). \tag{16}$$

An exact solution of Eq. (16) can be found for the case in which $M_z(x)$ and $M_x(x)$ are proportional to each other

$$M_x(x) = \alpha M_z(x) + m, \tag{17}$$

where α and m are real constants defined as

$$\alpha = \frac{M_x(-\infty) - M_x(+\infty)}{M_z(-\infty) - M_z(+\infty)}, \quad m = \frac{M_z(-\infty)M_x(+\infty) - M_z(+\infty)M_x(-\infty)}{M_z(-\infty) - M_z(+\infty)}. \tag{18}$$

Note that Eq. (17) is *exact* for the sharp corner shown in Fig. 3, for which M_x and M_z are the step-like functions of x.

As shown in the Supplementary Materials, under the condition of Eq. (17), the wave-function can be presented in the form

$$\Psi_{0D}(x) = \chi\psi(x), \tag{19}$$

where χ is the spin part of the wave function satisfying equation

$$\begin{pmatrix} -v_z\alpha + iv_0 & -v_z - iv_0\alpha \\ -v_z - iv_0\alpha & v_z\alpha - iv_0 \end{pmatrix}\chi = \nu\chi,$$

with eigenvalues $\nu = \pm\sqrt{1+\alpha^2}\sqrt{v_z^2 - v_0^2}$.

Then, by introducing a new variable $\tilde{x} = x/\sqrt{v_z^2 - v_0^2}$ and representing $\psi(x)$ in the form

$$\psi(x) = \tilde{\psi}(\tilde{x})e^{-i\tilde{x}\frac{(E-\varepsilon_0)v_0}{\sqrt{v_z^2 - v_0^2}}}, \tag{20}$$

we arrive at the equation for the coordinate part:

$$\left\{\hat{\tilde{k}}^2 + \tilde{W}(\tilde{x})^2 + \sigma\tilde{W}(\tilde{x})'\right\}\tilde{\psi}(\tilde{x}) = \varepsilon\tilde{\psi}(\tilde{x}), \tag{21}$$

where $\sigma = \pm 1$ (the sign of σ coincides with those for ν), and ε and $\tilde{W}(\tilde{x})$ are defined as

$$\begin{aligned} \varepsilon &= \frac{(E-\varepsilon_0)^2 v_z^2}{v_z^2 - v_0^2} - \frac{m^2}{1+\alpha^2}, \\ \tilde{W}(\tilde{x}) &= \sqrt{1+\alpha^2}M_z + \frac{m\alpha}{\sqrt{1+\alpha^2}}. \end{aligned} \tag{22}$$

Equation (21) possesses a special symmetry that corresponds to the formulation of supersymmetric quantum mechanics[57] with the supersymmetric potential $\tilde{W}(\tilde{x})$. If the signs of the asymptotes $\tilde{W}(+\infty)$ and $\tilde{W}(-\infty)$ are opposite, i.e.

$$\left(M_z(+\infty) + \frac{m\alpha}{1+\alpha^2}\right)\left(M_z(-\infty) + \frac{m\alpha}{1+\alpha^2}\right) < 0, \tag{23}$$

Eq. (21) always has a localized solution $\tilde{\psi}(\tilde{x})$ with $\varepsilon = 0$.

Thus, by means of Eqs. (20)–(23), the wave function of the corner state is written as:

$$\begin{aligned} \Psi_{0D}(x) = C &\begin{pmatrix} v_z\alpha - \sigma\sqrt{1+\alpha^2}\sqrt{v_z^2 - v_0^2} - iv_0 \\ v_z + iv_0\alpha \end{pmatrix} e^{-ix\frac{(E_{0D}-\varepsilon_0)v_0}{v_z^2 - v_0^2}} \\ &\times e^{\frac{\sigma}{\sqrt{1+\alpha^2}\sqrt{v_z^2 - v_0^2}}\int_0^x \{(1+\alpha^2)M_z(z) + m\alpha\}dz}, \end{aligned} \tag{24}$$

where C is the normalization constant and

$$E_{0D} = \varepsilon_0 + \frac{\sigma m}{\sqrt{1+\alpha^2}}\frac{\sqrt{v_z^2 - v_0^2}}{v_z}. \tag{25}$$

Note that in Eqs. (24) and (25), the sign of σ should be chosen in accordance with normalized condition of $\Psi_{0D}(x)$. If $\tilde{W}(+\infty) > 0, \sigma = -1$, while for $\tilde{W}(+\infty) < 0, \sigma = 1$. These two cases correspond to the internal and external corners at the same orientations of the two edges.

Let us make few remarks concerning the results obtained above. First, Eq. (23) can be also written in equivalent form

$$(M_z(+\infty) + \alpha M_x(+\infty))(M_z(-\infty) + \alpha M_x(-\infty)) < 0, \tag{26}$$

which is reduced to the well-known condition for the existence of the bound state in 1D Dirac system if one of the mass parameters M_z or M_x is absent.

Second, E_{0D} depends on the values of $\tilde{\beta}(-\infty)$ and $\tilde{\beta}(+\infty)$ as seen from Eq. (15). Nevertheless, since

$$(E_{0D} - \varepsilon_0)^2 < m_x(x)^2 + m_y(x)^2 \tag{27}$$

takes place for any values of $\tilde{\beta}(-\infty)$ and $\tilde{\beta}(+\infty)$, the corner state energy always lies in the band-gap of the edge states as soon as Eq. (26) is fulfilled. One can show that E_{0D} may formally achieve the energies of the 1D band edges at certain values of $\tilde{\beta}^*(-\infty)$ and $\tilde{\beta}^*(+\infty)$, corresponding to

$$\left(M_z^*(+\infty)+\alpha^* M_x^*(+\infty)\right)\left(M_z^*(-\infty)+\alpha^* M_x^*(-\infty)\right)=0.$$

The latter however represents the moment, when the corner state becomes delocalized.

Finally, we take into account the small terms proportional to v_x and v_y previously neglected in Eq. (12). The straightforward calculations on the basis of $\Psi_{0D}(x)$ (see Supplementary Materials) lead to the first-order energy shift:

$$\delta E_{0D}=-\frac{v_0 m}{v_z^2(1+\alpha^2)}\left[V(-\infty)\frac{\lambda(+\infty)}{\lambda(-\infty)+\lambda(\infty)}+V(+\infty)\frac{\lambda(-\infty)}{\lambda(-\infty)+\lambda(\infty)}\right], \tag{28}$$

where

$$\begin{aligned} V(x)&=(v_x+\alpha v_y)\cos 2\tilde{\beta}+(v_y-\alpha v_x)\sin 2\tilde{\beta},\\ \lambda(\pm\infty)&=\frac{(1+\alpha^2)M_z(\pm\infty)+m\alpha}{\sqrt{1+\alpha^2}\sqrt{v_z^2-v_0^2}}. \end{aligned} \tag{29}$$

One can verify that indeed $|\delta E_{0D}| \ll |E_{0D}|$ for both prototype QWs. The calculations for another Kramer's pair of the edge states described by $H_{1D}^*(-k_x-k_c,\theta,\varphi)$ results in the same energy of the corner state.

Trivial corner states. Let us now discuss the physical origin of the localized 0D corner state found above. Since it is clear from Eq. (15), the existence condition of Eq. (23) (or equivalently Eq. (26)) is fulfilled for different functions $m_x(x)$, $m_y(x)$ and $\tilde{\beta}(x)$. The function $\tilde{\beta}(x)$ characterizes the corner itself, while m_x and m_y include the characteristic of the entire system. Further, we show that, in the most general case, arising of 0D corner state simultaneously depends on the corner boundary conditions and the cubic symmetry of the system.

For a better understanding of the existence condition of Eq. (26), we first neglect the terms arising due to the cubic symmetry. In this case, one should set parameters $R_{1,2}^{(a)}$ and $\tilde{R}_{1,2}^{(a)}$ of 2D Hamiltonian in Eq. (5) to zero also resulting in the zero values of F_a and $\tilde{F}_a$ in Eq. (11). The latter, in turn, leads to the vanishing of m_y, v_y and δ_y in Eq. (10), while m_x, v_x and δ_x become independent of x. Thus, in the absence of the cubic symmetry, by means of Eqs. (15) and (18), the existence condition of Eq. (26) is reduced to

$$-\frac{4\sin^4(\beta_1-\beta_2)}{(\sin 2\beta_1-\sin 2\beta_2)^2}<0, \tag{30}$$

where $\beta_1=\tilde{\beta}(x=-\infty)$ and $\beta_2=\tilde{\beta}(x=+\infty)$ chosen in accordance with Eq. (13). Since it is easy to see, the localized corner state exists if $\beta_1\neq\beta_2$. These parameters can be given a precise physical interpretation.

Let us consider a δ-function electrostatic potential at $x=0$. Then, if we integrate the Schrödinger equation with $\tilde{H}_{1D}(\delta k,x)+V_0\delta(0)\mathbf{I}_2$ (where V_0 is a real parameter) in the range of $-\eta\leq x\leq\eta$ (where η is a positive infinitesimal quantity), we directly obtain Eq. (13) with $\beta_2-\beta_1=V_0 v_z/(v_z^2-v_0^2)$. Therefore, $\beta_1\neq\beta_2$ can be interpreted as the presence of δ-like electrostatic potential localized at the corner. Thus, the corner states arising in this case are topologically trivial, since they are independent of the cubic symmetry of the system. We also note their independence of the sign of V_0, as clearly seen from Eq. (30).

Topological corner states. We now focus on the opposite case, when there is no potential barrier at the corner i.e. $\beta_1=\beta_2$. As seen from Eq. (13), these parameters can be both set to zero without loss of generality, which leads to $M_x(x,0)=m_x(x)$ and $M_z(x,0)=-m_y(x)$. In this case, the presence of the corner states is governed by the cubic symmetry of 2D system, represented by the non-zero values of F_a and $\tilde{F}_a$ in Eq. (11). The latter means that the picture of the symmetry-protected corner states should strongly depends not only on crystallographic orientations of the meeting edges but also on the QW growth direction.

Figure 4A,B present the calculations for the prototype QWs with double band inversion grown along (001) crystallographic orientation (see the diagrams in Fig. 1). For both QWs, the angles φ_1 and φ_2 defining the corner orientation in Fig. 3A are chosen to be $\varphi_1=\pi/3$ and $\varphi_2=2\pi/3$, while θ in Eq. (10) is assumed to be zero. One can verify that the condition of existence of Eq. (26) is fulfilled for these angles, and, therefore, the corner states arise in the system. As seen from Fig. 4A,B, due to the relationship between $m_x(\varphi)$ and $m_y(\varphi)$, the localized energies for internal $\sigma=+1$ and external $\sigma=-1$ corners are very close to the extrema of 1D dispersion of the edge states.

Figure 4C,D represent the angle diagram showing the edge orientations in the (001)-oriented prototype QWs, for which the existence condition of Eq. (26) is valid. It is seen that the values of φ_1 and φ_2 yielding the corner states are qualitatively represented as the grey regions elongated along the lines defined by

$$\varphi_1+\varphi_2=n_0(2\pi/4), \tag{31}$$

excluding the points lying at verticals and horizontals corresponding to $\varphi_1=m_0\pi/4$ and $\varphi_2=l_0\pi/4$, where n_0, m_0 and l_0 are integers. As seen from Fig. 3A, the 2D system edges at these angles, coincides with [110], [1$\bar{1}$0], [100] or [010] crystallographic planes, being the faces of (001)-oriented QWs in this case. Since we have neglected the terms resulting from possible breaking of inversion symmetry in the system, the (001)-oriented prototype QWs

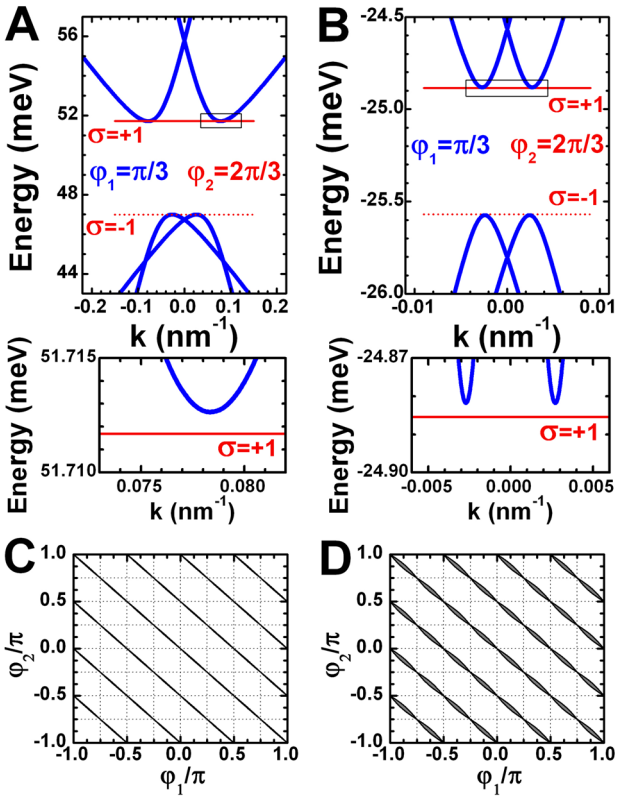

Figure 4. Topological corner states in (001)-oriented prototype QWs. (**A**,**B**) 1D dispersion of the edge states (in blue) for the boundary oriented at $\varphi_1 = \pi/3$ and the corner states energy $E_{0D} + \delta E_{0D}$ (in red) formed by the second boundary oriented at $\varphi_2 = 2\pi/3$. The (**A**) and (**B**) correspond to the (001) three-layer InAs/GaInSb (**A**) and double HgTe/CdHgTe QWs, respectively. The layer thicknesses of the QWs are marked by the red symbols in Fig. 1B,C. (**C**,**D**) The phase diagram for the presence (grey region) and absence (white region) of topological corner states in the three-layer InAs/GaInSb and double HgTe/CdHgTe QWs as a function of the two edge orientations. In the grey regions, the existence condition of Eq. (26) at $\beta_1 = \beta_2 = 0$ is fulfilled. The vertical and horizontal thin dotted lines represent the angles when the edges of 2D system, which are actually the faces of (001)-oriented QWs, coincide with [110], [1$\bar{1}$0], [100] and [010] crystallographic planes.

preserve the mirror symmetry about the mentioned planes. Therefore, one concludes that if one of the QW edge coincides with the mirror symmetry planes, the corner states are absent in the system.

In light of the above, Eq. (31) describes the corners, whose bisector corresponds to the one of the mirror symmetry planes. The latter results in reflection symmetry of the angle diagram with respect to the lines described by Eq. (31). As expected from the four-fold rotational symmetry of (001)-oriented QWs with respect to the growth direction, the angle pattern in Fig. 4C,D also possess a $\pi/2$-periodicity in φ_1 and φ_2.

So far, we have discussed the case of (001)-oriented QWs, by whose example we have shown a direct relationship between topological corner states and the symmetry elements of the QW. As the inversion symmetry is preserved in our model, the (001)-oriented QWs have the point group D_{4h} origin from the point group O_h of bulk multi-band $\mathbf{k}\cdot\mathbf{p}$ Hamiltonian (see Supplementary Materials). Obviously, if one reduces the symmetry of 2D system, the picture of the corner states should change as well. Further, we consider C_{2h}-symmetric QWs grown along (013) crystallographic direction inspired by recent experimental investigations of double HgTe QWs of the same orientation[58–60].

Figure 5A,B provide the angle diagram of topological corner states in the prototypes three-layer InAs/GaInSb and double HgTe/CdHgTe QWs oriented along (013) crystallographic direction. The calculations are performed by assuming $\theta = \arctan(m/n)$ in Eq. (10) with $(m, n) = (1, 3)$. It is seen that the values of φ_1 and φ_2, for which the existence condition is fulfilled, represent significantly different picture of the corner states than the one for (001)-oriented QWs.

We first note π-periodicity in φ_1 and φ_2 of the angle pattern due to the two-fold rotational symmetry of (0mn)-oriented QWs in contrast to the $\pi/2$-periodicity of (001)-oriented 2D systems. Second, due to the symmetry lowering, (013)-oriented QWs have only two [100] and [03$\bar{1}$] mirror planes perpendicular to the QW plane. These planes are represented by dotted verticals and horizontals at $\varphi_1 = m_0\pi/2$ and $\varphi_2 = l_0\pi/2$ in Fig. 5A,B. It is seen that the corner states are absent if one of the QW edge coincides with the mirror symmetry planes. Finally, in contrast to (001)-oriented QWs, (0mn)-oriented QWs possess the corner states if one of the edges is at $\pi/4°$ with respect to the (100) crystallographic axis. The latter is clearly seen in Fig. 5C, which shows the negative values of the function illustrating the existence condition of Eq. (26) for the corner states.

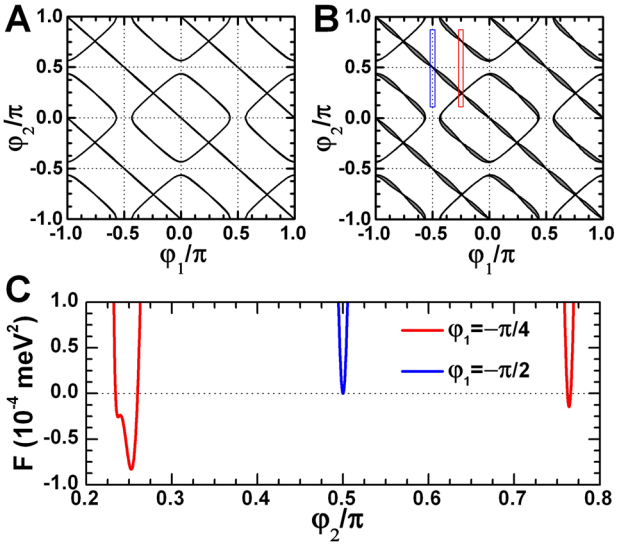

Figure 5. Topological corner states in (013)-oriented prototype QWs. (**A**,**B**) The phase diagram for the presence (grey region) and absence (white region) of 0D topological corner states in the three-layer InAs/GaInSb (**A**) and double HgTe/CdHgTe QWs (**B**) as a function of the two edge orientations. The vertical and horizontal thin dotted lines represent the angles when the edges of 2D system coincide with [100] and $[03\bar{1}]$ crystallographic planes. (**C**) The function $F(\varphi_1,\varphi_2) = (M_z(\varphi_1) + \alpha M_x(\varphi_1))(M_z(\varphi_2) + \alpha M_x(\varphi_2))$ representing the existence condition of Eq. (26) at $\beta_1 = \beta_2 = 0$ in the ranges marked with colored rectangles in (**B**). The dotted line marks the zero value.

Discussion

To summarize, we have investigated the existence conditions for 0D corner states in cubic semiconductor QWs with double band inversion. We have demonstrated that 0D corner states in such 2D system can appear either due to the presence of electrostatic potential localized in the corner, or due to the crystalline symmetry of the QW. The former case can be physically interpreted as the impurity potential resulting in trivial corner states. The latter corresponds to the symmetry-induced corner states inherent for 2D HOTI state in cubic semiconductor QWs with double band inversion. We have shown that the corners hosting 0D topological states depend not only on crystallographic orientations of the meeting edges but also on the growth orientation and parameters of the QWs.

Let us now make a few remarks concerning the approximation used in this work. As it is clear from the above, theoretical investigations were performed on the basis of multi-band $\mathbf{k}\cdot\mathbf{p}$ Hamiltonian[49] for the envelope Bloch functions, which is indeed valid on scales much larger than the unit cell. In this case, all functions that are changed on a scale comparable to the unit cell are considered as step-like or delta-functions. In this sense, a meeting point of the corner shown in Fig. 3A represents a 2D unit cell at the corner of an effective 2D system in the QW plane. The special arrangement of atoms in the vicinity of the corner preserving C_n symmetry of the bulk may lead to the fractional charge of the corner states, known as a fractional corner anomaly[22,23,61–63]. We note that since fractional corner anomaly requires a theoretical description on the unit cell scale, it cannot be treated on the basis of multi-band $\mathbf{k}\cdot\mathbf{p}$ Hamiltonian.

Throughout the work, we have neglected the inversion symmetry breaking terms resulting from anisotropy of chemical bonds at the QW interfaces[54] and possible bulk inversion asymmetry of the unit cell[55]. The former is known as an interface inversion asymmetry[54], while the latter causes the difference between O_h and T_d point groups of diamond and zinc-blende semiconductors. Taking into account these additional terms in bulk $\mathbf{k}\cdot\mathbf{p}$ Hamiltonian leads to the non-diagonal blocks of the effective 2D Hamiltonian $H_{2D}(k_x, k_y)$ in Eq. (1). Since the inversion symmetry breaking terms do not affect the very fact of double band inversion, their presence will modify only the edge state parameters $v_x, v_y, m_x, m_y, \delta_x, \delta_y$ keeping the form of 1D edge Hamiltonian in Eq. (9).

For instance, taking into account the interface and bulk inversion asymmetry in (001)-oriented zinc-blende semiconductor QW reduces the point symmetry from D_{4h} to C_{2v}[54], which, in their turn, also changes the periodicity of $v_x(\varphi)$, $v_y(\varphi)$, $m_x(\varphi)$, $m_y(\varphi)$, $\delta_x(\varphi)$, $\delta_y(\varphi)$ in Eq. (9) from $\pi/2$ to π. In this case, the symmetry-induced corner states will arise at the corner with the meeting edges, whose orientations differ from those shown in Fig. 4. For the prototype InAs/GaInSb and HgTe/CdHgTe QWs considered in this work, the terms due to interface and bulk inversion asymmetry are small and induce therefore only a slight modification of the phase diagrams.

We emphasize that since the presence of the corner states depends on the mutual ratio between m_x and m_y, one may find the QW orientation and strength of inversion-symmetry breaking terms, for which the existence condition of Eq. (26) cannot be fulfilled. The study of all possible cases of violation of Eq. (26) is however out the scope of our work first considering the QWs based on IV, II–VI and III–V semiconductors, in which inversion-symmetry breaking terms are usually small.

Finally, we stress the importance of theoretical results obtained in this work in view of possible applications and their impact on further experimental investigations. After the tremendous interest in II–VI and III–V

semiconductor QWs induced by prediction and observation of QSHI[39–41], our work shows the importance of cubic semiconductor QWs for the realization of high-order topological states as well. In view of mature growth of IV, II–IV and III–V semiconductor QWs on Si-wafers[64,65] as well as device fabrication technology, our results provide an important first step to future realistic electronics operating on the basis of higher-order topological states including higher-order topological superconductors in hybrid devices[66,67].

Methods

Band structure calculations were performed by using multi-band $\mathbf{k}\cdot\mathbf{p}$ Hamiltonian[49], which directly takes into account the interactions between Γ_6, Γ_8, and Γ_7 bands in bulk materials. This model well describes the electronic states in a wide range of narrow-gap semiconductor QWs, particularly in the InAs/GaInSb[46,48] and HgTe/CdHgTe QWs[58–60]. In the multi-band $\mathbf{k}\cdot\mathbf{p}$ Hamiltonian, we also took into account the terms, describing the strain effect arising because of the mismatch of lattice constants in the buffer, QW layers, and barriers. The calculations had been performed by expanding the eight-component envelope wave functions in the basis set of plane waves and by numerical solution of the eigenvalue problem. Details of calculations and the form of the Hamiltonian can be found in the study of Krishtopenko et al.[49]. Parameters for the bulk materials and valence band offsets for the the InAs/GaInSb and HgTe/CdHgTe QWs used in the calculations are provided in Ref.[50] and Ref.[49], respectively. To derive effective 2D Hamiltonian valid in the vicinity of the Γ point from the multi-band $\mathbf{k}\cdot\mathbf{p}$ Hamiltonian, we implied the procedure proposed by Bernevig et al.[2] and described in details in the Supplementary Materials.

Received: 22 May 2021; Accepted: 7 October 2021
Published online: 26 October 2021

References

1. Kane, C. L. & Mele, E. J. Z_2 topological order and the quantum spin hall effect. *Phys. Rev. Lett.* **95**, 146802. https://doi.org/10.1103/PhysRevLett.95.146802 (2005).
2. Bernevig, B. A., Hughes, T. L. & Zhang, S.-C. Quantum spin hall effect and topological phase transition in hgte quantum wells. *Science* **314**, 1757–1761. https://doi.org/10.1126/science.1133734 (2006).
3. Hasan, M. Z. & Kane, C. L. Colloquium: Topological insulators. *Rev. Mod. Phys.* **82**, 3045–3067. https://doi.org/10.1103/RevModPhys.82.3045 (2010).
4. Qi, X.-L. & Zhang, S.-C. Topological insulators and superconductors. *Rev. Mod. Phys.* **83**, 1057–1110. https://doi.org/10.1103/RevModPhys.83.1057 (2011).
5. Bansil, A., Lin, H. & Das, T. Colloquium: Topological band theory. *Rev. Mod. Phys.* **88**, 021004. https://doi.org/10.1103/RevModPhys.88.021004 (2016).
6. Bradlyn, B. *et al.* Beyond Dirac and Weyl fermions: Unconventional quasiparticles in conventional crystals. *Science* **353**, aaf5037. https://doi.org/10.1126/science.aaf5037 (2016).
7. Bradlyn, B. *et al.* Topological quantum chemistry. *Nature* **547**, 298–305. https://doi.org/10.1038/nature23268 (2017).
8. Po, H. C., Vishwanath, A. & Watanabe, H. Symmetry-based indicators of band topology in the 230 space groups. *Nat. Commun.* **8**, 50. https://doi.org/10.1038/s41467-017-00133-2 (2017).
9. Benalcazar, W. A., Bernevig, B. A. & Hughes, T. L. Quantized electric multipole insulators. *Science* **357**, 61–66. https://doi.org/10.1126/science.aah6442 (2017).
10. Langbehn, J., Peng, Y., Trifunovic, L., von Oppen, F. & Brouwer, P. W. Reflection-symmetric second-order topological insulators and superconductors. *Phys. Rev. Lett.* **119**, 246401. https://doi.org/10.1103/PhysRevLett.119.246401 (2017).
11. Song, Z., Fang, Z. & Fang, C. $(d-2)$-dimensional edge states of rotation symmetry protected topological states. *Phys. Rev. Lett.* **119**, 246402. https://doi.org/10.1103/PhysRevLett.119.246402 (2017).
12. Schindler, F. *et al.* Higher-order topological insulators. *Sci. Adv.* **4**, eaat0346. https://doi.org/10.1126/sciadv.aat0346 (2018).
13. Ezawa, M. Higher-order topological insulators and semimetals on the breathing kagome and pyrochlore lattices. *Phys. Rev. Lett.* **120**, 026801. https://doi.org/10.1103/PhysRevLett.120.026801 (2018).
14. Khalaf, E. Higher-order topological insulators and superconductors protected by inversion symmetry. *Phys. Rev. B* **97**, 205136. https://doi.org/10.1103/PhysRevB.97.205136 (2018).
15. Yan, Z., Song, F. & Wang, Z. Majorana corner modes in a high-temperature platform. *Phys. Rev. Lett.* **121**, 096803. https://doi.org/10.1103/PhysRevLett.121.096803 (2018).
16. Schindler, F. *et al.* Higher-order topology in bismuth. *Nat. Phys.* **15**, 918–924. https://doi.org/10.1038/s41567-018-0224-7 (2018).
17. Noguchi, R. *et al.* Evidence for a higher-order topological insulator in a three-dimensional material built from van der Waals stacking of bismuth-halide chains. *Nat. Mater.*https://doi.org/10.1038/s41563-020-00871-7 *(2021).*
18. Choi, Y.-B. *et al.* Evidence of higher-order topology in multilayer wte_2 from Josephson coupling through anisotropic hinge states. *Nat. Mater.*https://doi.org/10.1038/s41563-020-0721-9 *(2020).*
19. Kononov, A. *et al.* One-dimensional edge transport in few-layer wte_2. *Nano Lett.* **20**, 4228–4233. https://doi.org/10.1021/acs.nanolett.0c00658 (2020).
20. Wang, Z., Wieder, B. J., Li, J., Yan, B. & Bernevig, B. A. Higher-order topology, monopole nodal lines, and the origin of large fermi arcs in transition metal dichalcogenides xte_2 (x = Mo, W). *Phys. Rev. Lett.* **123**, 186401. https://doi.org/10.1103/PhysRevLett.123.186401 (2019).
21. Fang, Y. & Cano, J. Higher-order topological insulators in antiperovskites. *Phys. Rev. B* **101**, 245110. https://doi.org/10.1103/PhysRevB.101.245110 (2020).
22. Peterson, C. W., Li, T., Benalcazar, W. A., Hughes, T. L. & Bahl, G. A fractional corner anomaly reveals higher-order topology. *Science* **368**, 1114–1118. https://doi.org/10.1126/science.aba7604 (2020).
23. Peterson, C. W., Li, T., Jiang, W., Hughes, T. L. & Bahl, G. Trapped fractional charges at bulk defects in topological insulators. *Nature* **589**, 376–380. https://doi.org/10.1038/s41586-020-03117-3 (2021).
24. Peterson, C. W., Benalcazar, W. A., Hughes, T. L. & Bahl, G. A quantized microwave quadrupole insulator with topologically protected corner states. *Nature* **555**, 346–350. https://doi.org/10.1038/nature25777 (2018).
25. Serra-Garcia, M. *et al.* A quantized microwave quadrupole insulator with topologically protected corner states. *Nature* **555**, 342–345. https://doi.org/10.1038/nature25156 (2018).
26. Imhof, S. *et al.* Topolectrical-circuit realization of topological corner modes. *Nat. Phys.* **14**, 925–929. https://doi.org/10.1038/s41567-018-0246-1 (2018).
27. Noh, J. *et al.* Topological protection of photonic mid-gap defect modes. *Nat. Photonics* **12**, 408–415. https://doi.org/10.1038/s41566-018-0179-3 (2018).

28. Xue, H., Yang, Y., Gao, F., Chong, Y. & Zhang, B. Acoustic higher-order topological insulator on a kagome lattice. *Nat. Mater.* **18**, 108–112. https://doi.org/10.1038/s41563-018-0251-x (2019).
29. Ni, X., Weiner, M., Alù, A. & Khanikaev, A. B. Observation of higher-order topological acoustic states protected by generalized chiral symmetry. *Nat. Mater.* **18**, 113–120. https://doi.org/10.1038/s41563-018-0252-9 (2019).
30. Mittal, S. *et al.* Photonic quadrupole topological phases. *Nat. Photonics* **13**, 692–696. https://doi.org/10.1038/s41566-019-0452-0 (2019).
31. Hassan, A. E. *et al.* Corner states of light in photonic waveguides. *Nat. Photonics* **13**, 697–700. https://doi.org/10.1038/s41566-019-0519-y (2019).
32. Zhang, X. *et al.* Second-order topology and multidimensional topological transitions in sonic crystals. *Nat. Phys.* **15**, 582–588. https://doi.org/10.1038/s41567-019-0472-1 (2019).
33. Xie, B.-Y. *et al.* Visualization of higher-order topological insulating phases in two-dimensional dielectric photonic crystals. *Phys. Rev. Lett.* **122**, 233903. https://doi.org/10.1103/PhysRevLett.122.233903 (2019).
34. Chen, X.-D. *et al.* Direct observation of corner states in second-order topological photonic crystal slabs. *Phys. Rev. Lett.* **122**, 233902. https://doi.org/10.1103/PhysRevLett.122.233902 (2019).
35. Ezawa, M. Minimal models for Wannier-type higher-order topological insulators and phosphorene. *Phys. Rev. B* **98**, 045125. https://doi.org/10.1103/PhysRevB.98.045125 (2018).
36. Sheng, X.-L. *et al.* Two-dimensional second-order topological insulator in graphdiyne. *Phys. Rev. Lett.* **123**, 256402. https://doi.org/10.1103/PhysRevLett.123.256402 (2019).
37. Chen, C. *et al.* Universal approach to magnetic second-order topological insulator. *Phys. Rev. Lett.* **125**, 056402. https://doi.org/10.1103/PhysRevLett.125.056402 (2020).
38. Park, M. J., Kim, Y., Cho, G. Y. & Lee, S. Higher-order topological insulator in twisted bilayer graphene. *Phys. Rev. Lett.* **123**, 216803. https://doi.org/10.1103/PhysRevLett.123.216803 (2019).
39. König, M. *et al.* The quantum spin hall effect: Theory and experiment. *J. Phys. Soc. Jpn.* **77**, 031007. https://doi.org/10.1143/JPSJ.77.031007 (2008).
40. Liu, C., Hughes, T. L., Qi, X.-L., Wang, K. & Zhang, S.-C. Quantum spin hall effect in inverted type-II semiconductors. *Phys. Rev. Lett.* **100**, 236601. https://doi.org/10.1103/PhysRevLett.100.236601 (2008).
41. Knez, I., Du, R.-R. & Sullivan, G. Evidence for helical edge modes in inverted InAs/GaSb quantum wells. *Phys. Rev. Lett.* **107**, 136603. https://doi.org/10.1103/PhysRevLett.107.136603 (2011).
42. Miao, M. S. *et al.* Polarization-driven topological insulator transition in a GaN/InN/GaN quantum well. *Phys. Rev. Lett.* **109**, 186803. https://doi.org/10.1103/PhysRevLett.109.186803 (2012).
43. Zhang, D., Lou, W., Miao, M., Zhang, S.-C. & Chang, K. Interface-induced topological insulator transition in GaAs/Ge/GaAs quantum wells. *Phys. Rev. Lett.* **111**, 156402. https://doi.org/10.1103/PhysRevLett.111.156402 (2013).
44. Candido, D. R., Flatté, M. E. & Egues, J. C. Blurring the boundaries between topological and nontopological phenomena in dots. *Phys. Rev. Lett.* **121**, 256804. https://doi.org/10.1103/PhysRevLett.121.256804 (2018).
45. Du, L. *et al.* Tuning edge states in strained-layer InAs/GaInSb quantum spin hall insulators. *Phys. Rev. Lett.* **119**, 056803. https://doi.org/10.1103/PhysRevLett.119.056803 (2017).
46. Krishtopenko, S. S. *et al.* Temperature-dependent terahertz spectroscopy of inverted-band three-layer InAs/GaSb/InAs quantum well. *Phys. Rev. B* **97**, 245419. https://doi.org/10.1103/PhysRevB.97.245419 (2018).
47. Suchalkin, S. *et al.* Engineering Dirac materials: Metamorphic $\mathrm{inas}_{1-x}\mathrm{sb}_x/\mathrm{inas}_{1-y}\mathrm{sb}_y$ superlattices with ultralow bandgap. *Nano Lett.* **18**, 412–417. https://doi.org/10.1021/acs.nanolett.7b04304 (2018).
48. Krishtopenko, S. S. *et al.* Massless Dirac fermions in III–V semiconductor quantum wells. *Phys. Rev. B* **99**, 121405. https://doi.org/10.1103/PhysRevB.99.121405 (2019).
49. Krishtopenko, S. S. *et al.* Pressure- and temperature-driven phase transitions in HgTe quantum wells. *Phys. Rev. B* **94**, 245402. https://doi.org/10.1103/PhysRevB.94.245402 (2016).
50. Krishtopenko, S. S. & Teppe, F. Quantum spin hall insulator with a large bandgap, Dirac fermions, and bilayer graphene analog. *Sci. Adv.* **4**, eaap7529. https://doi.org/10.1126/sciadv.aap7529 (2018).
51. Krishtopenko, S. S., Knap, W. & Teppe, F. Phase transitions in two tunnel-coupled HgTe quantum wells: Bilayer graphene analogy and beyond. *Sci. Rep.* **6**, 30755. https://doi.org/10.1038/srep30755 (2016).
52. Krishtopenko, S. S. & Teppe, F. Realistic picture of helical edge states in HgTe quantum wells. *Phys. Rev. B* **97**, 165408. https://doi.org/10.1103/PhysRevB.97.165408 (2018).
53. Krishtopenko, S. S., Antezza, M. & Teppe, F. Disorder-induced phase transition in Dirac systems beyond the linear approximation. *Phys. Rev. B* **101**, 205424. https://doi.org/10.1103/PhysRevB.101.205424 (2020).
54. Ivchenko, E. L., Kaminski, A. Y. & Rössler, U. Heavy-light hole mixing at zinc-blende (001) interfaces under normal incidence. *Phys. Rev. B* **54**, 5852–5859. https://doi.org/10.1103/PhysRevB.54.5852 (1996).
55. Dresselhaus, G. Spin-orbit coupling effects in zinc blende structures. *Phys. Rev.* **100**, 580–586. https://doi.org/10.1103/PhysRev.100.580 (1955).
56. Wada, M., Murakami, S., Freimuth, F. & Bihlmayer, G. Localized edge states in two-dimensional topological insulators: Ultrathin Bi films. *Phys. Rev. B* **83**, 121310. https://doi.org/10.1103/PhysRevB.83.121310 (2011).
57. Witten, E. Dynamical breaking of supersymmetry. *Nucl. Phys. B* **188**, 513–554. https://doi.org/10.1016/0550-3213(81)90006-7 (1981).
58. Bovkun, L. S. *et al.* Magnetospectroscopy of double HgTe/CdHgTe quantum wells. *Semiconductors* **50**, 1532–1538. https://doi.org/10.1134/S1063782616110063 (2016).
59. Yakunin, M. V. *et al.* Unconventional reentrant quantum hall effect in a HgTe/CdHgTe double quantum well. *Phys. Rev. B* **102**, 165305. https://doi.org/10.1103/PhysRevB.102.165305 (2020).
60. Gusev, G. M. *et al.* Two-dimensional topological insulator state in double HgTe quantum well. *Phys. Rev. B* **101**, 241302. https://doi.org/10.1103/PhysRevB.101.241302 (2020).
61. Benalcazar, W. A., Li, T. & Hughes, T. L. Quantization of fractional corner charge in C_n-symmetric higher-order topological crystalline insulators. *Phys. Rev. B* **99**, 245151. https://doi.org/10.1103/PhysRevB.99.245151 (2019).
62. Zhu, P., Loehr, K. & Hughes, T. L. Identifying C_n-symmetric higher-order topology and fractional corner charge using entanglement spectra. *Phys. Rev. B* **101**, 115140. https://doi.org/10.1103/PhysRevB.101.115140 (2020).
63. Li, T., Zhu, P., Benalcazar, W. A. & Hughes, T. L. Fractional disclination charge in two-dimensional C_n-symmetric topological crystalline insulators. *Phys. Rev. B* **101**, 115115. https://doi.org/10.1103/PhysRevB.101.115115 (2020).
64. Cornet, C. *et al.* Zinc-blende group III–V/group IV epitaxy: Importance of the miscut. *Phys. Rev. Mater.* **4**, 0153401. https://doi.org/10.1103/PhysRevMaterials.4.053401 (2020).
65. Loghmari, Z. *et al.* InAs-based quantum cascade lasers grown on on-axis (001) silicon substrate. *APL Photonics* **5**, 041302. https://doi.org/10.1063/5.0002376 (2020).
66. Hsu, C.-H., Stano, P., Klinovaja, J. & Loss, D. Majorana Kramers pairs in higher-order topological insulators. *Phys. Rev. Lett.* **121**, 196801. https://doi.org/10.1103/PhysRevLett.121.196801 (2018).
67. Yan, Z. Majorana corner and hinge modes in second-order topological insulator/superconductor heterostructures. *Phys. Rev. B* **100**, 205406. https://doi.org/10.1103/PhysRevB.100.205406 (2019).

Acknowledgements
The author is grateful to Frédéric Teppe from Laboratoire Charles Coulomb for helpful discussions on the manuscript. This work was partially supported by the Foundation for Polish Science: the IRAP program (Grant No. MAB/2018/9, project CENTERA), by MIPS department of Montpellier University through the "Occitanie Terahertz Platform", by CNRS through IRP "TeraMIR" and by the French Agence Nationale pour la Recherche (Colector project).

Author contributions
S.S.K. conceived and supervised the project and also did analytical and numerical calculations. The figures were prepared by S.S.K. The paper and the Supplementary Materials were prepared by S.S.K.

Competing interests
The author declares no competing interests.

Additional information
Supplementary Information The online version contains supplementary material available at https://doi.org/10.1038/s41598-021-00577-z.

Correspondence and requests for materials should be addressed to S.S.K.

Reprints and permissions information is available at www.nature.com/reprints.

Publisher's note Springer Nature remains neutral with regard to jurisdictional claims in published maps and institutional affiliations.